Tuning substrate temperature for improved adhesion and mechanical properties of magnetron sputtered high entropy alloy thin-films

Thin Solid Films 832 (2025) 140817

Contents lists available at ScienceDirect

Thin Solid Films

journal homepage: www.elsevier.com/locate/tsf

Tuning substrate temperature for improved adhesion and mechanical properties of magnetron sputtered high entropy alloy thin-films

M. Subhakar [a], L. Pandey [b,e], S. Chaudhary [b], S.P. Jaiswal [c], S.S. Singh [c], U. Mahmud [d], Y.L. Chiu [d], I.P. Jones [d], J. Jain [a,*]

[a] Department of Materials Science and Engineering, Indian Institute of Technology Delhi, New Delhi 110016, India
[b] Thin Film Laboratory, Department of Physics, Indian Institute of Technology Delhi, New Delhi 110016, India
[c] Department of Material Science and Engineering, Indian Institute of Technology Kanpur, Uttar Pradesh 208016, India
[d] School of Metallurgy and Materials, University of Birmingham, Edgbaston, Birmingham B15 2TT, UK
[e] Department of Microtechnology and Nanoscience, Chalmers University of Technology, SE-41296 Göteborg, Sweden

ARTICLE INFO

Keywords:
Thin film
High entropy alloy
Magnetron sputtering
Interface chemistry
Adhesion mechanism

ABSTRACT

This work reports on the deposition of non-equiatomic CoCrFeNi high entropy alloy (HEA) thin films at various substrate temperatures (Room Temperature (RT), 200 °C, 300 °C, and 400 °C) on EN-24 steel substrates. The deposited films exhibited a preferred {111} crystallographic orientation and possessed a single-phase face centred cubic (FCC) crystal structure. The roughness of the film (R_{rms}) gradually increased from ~ 1 nm to ~ 4 nm as the particle size grew from ~ 20 nm to ~ 37 nm simultaneously as the substrate temperature increased from 200 °C to 400 °C, indicating an enhancement in atomic mobility across intergranular interfaces. The hardness of the film reached to a maximum of ~ 17 GPa for the film fabricated at 400 °C. This increase is attributed to improved crystallinity, preferential growth orientation and higher columnar density. Notice that this hardness significantly exceeded that of steel substrate, nearly fourfold. The films deposited at 200 °C and 300 °C exhibited the exceptional adhesion in the incremental load scratch tests, with no signs of delamination. On the other hand, the films deposited at room temperature and 400 °C delaminated during the scratch test. The diffusion bond established between the film and the substrate contributed significantly towards the outstanding adhesion of the film, as evidenced by the cross-sectional Transmission Electron Microscopy (TEM) analysis.

1. Introduction

In conventional alloys, one or two elements typically form a matrix with minor solute amounts influencing their properties [1]. However, in 2004, Yeh et al. [2] introduced the concept of high entropy alloys (HEA) and Cantor et al. [3] termed a similar class of alloys as multi-component principal element alloys that are particularly fascinating because of their excellent and unusual properties which arise from their unique compositional state where five or more primary elements added in equimolar or non-equimolar ratios, with each element's content ranging from 5–35 % [2]. The basis for the name comes from the high configurational entropy as they are claimed to favor the formation of simple solid solution phases like body centred cubic (BCC), face centred cubic (FCC), or Hexagonal closed packing (HCP) rather than any intermetallic phases [4,5]. These HEAs are known to have outstanding wear and corrosion resistance [6], high yield strength [7–9], large ductility [10], excellent fatigue resistance [11] and good fracture toughness [12,13]. Thus, these alloys are of special interest to researchers.

Over the last two decades, HEAs have been widely studied in the bulk form leading to significant advances in understanding their unique properties [14–16]. However, significant knowledge on HEA thin films remails relatively limited and many aspects of their behaviour are not fully understood [17,18]. It has been reported that HEAs when fabricated as thin films show high hardness [19] because of their nanocrystalline structure, and improved wear resistance [20]. This enhanced hardness and the associated mechanical properties make HEA thin films highly attractive as protective coatings.

The application of thin-film protective coatings is promising for increasing the lifespan of engineering components, especially in demanding fields of aerospace [21], mechanical components [22] and many other crucial engineering applications [23–25].

The common methods to deposit thin films are laser cladding,

* Corresponding author. .
E-mail address: jayantj@iitd.ac.in (J. Jain).

https://doi.org/10.1016/j.tsf.2025.140817
Received 28 July 2025; Received in revised form 7 October 2025; Accepted 25 October 2025
Available online 26 October 2025

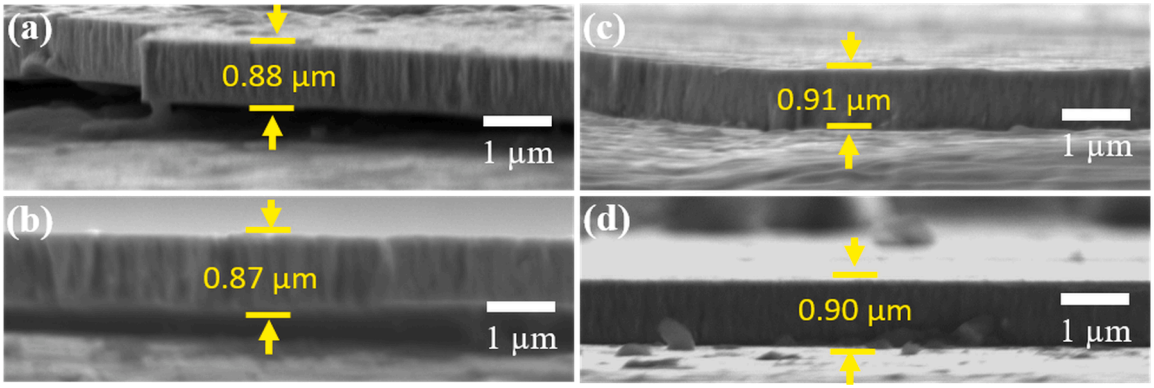

Fig. 1. Cross-sectional SEM images of non-equiatomic CoCrFeNi thin films deposited at (a) RT, (b) 200 °C, (c) 300 °C, and (d) 400 °C (The images show films exhibiting columnar growth morphology of thin films with a thickness of ~ 0.9 μm).

magnetron sputtering, spraying and electro-deposition [26]. Among these, Magnetron sputtering is one of the most favoured fabrication techniques due to its ability to precisely control the microstructure, film chemistry and physical features through tweaking of deposition parameters. These sputtered films possess the advantages of strong bonding force, dense and uniform structure, and enhanced strengthening caused by homogeneous solid solution [19,27,28].

Khan et al. [29] deposited $AlCoCrCu_{0.5}FeNi$ films onto Si (100) substrates at varying radio frequency (RF) powers (200 W, 250 W and 300 W). The resulting films were polycrystalline, exhibiting a mixture of FCC and BCC phases. Notably, the BCC fraction increased with an increase in the substrate power. The High-resolution transmission electron microscopy (HR-TEM) results revealed the presence of amorphous phase at the grain boundaries. Additionally, grain morphology evolved from equiaxed to columnar as the substrate power increased from 200 W to 300 W. The highest achieved hardness of 13 GPa was attributed to the reduced particle size and increased Al content in the fabricated films. Alternatively, Zhao et al. [30] investigated the deposition of CoCrFeNi films under varying bias voltages. They found that the films displayed a columnar morphology with a combination of FCC and amorphous phases. The maximum hardness, approximately 12 GPa, was observed in the film produced at a bias voltage of −200 V.

Similarly, Hu et al. [31] investigated the impact of substrate temperature on Fe-Co-Ni-Cr-Mn films deposited on Si substrates. They observed that the hardness initially increased with temperature due to a reduction in voids at the grain boundaries but then decreased as the particle size increased. Additionally, they noted a decrease in the fraction of amorphous phase within crystalline matrix as the substrate temperature increased, while the crystallinity of the films improved with higher substrate temperatures.

While most studies have been carried out utilizing Si substrates [29–31], there are limited number of studies focusing on using steel substrates. For instance, Zhao et al. [32] fabricated $AlCrFeCoNiCu_{0.5}$ HEA thin films on stainless steel 304 substrates with varying bias voltages using filtered cathodic arc deposition. Their primary objective was to investigate both interface and surface chemistry. All films exhibited an FCC phase with predominantly equiaxed grains, and the maximum film hardness reached ~ 9 GPa at −25 V. As the bias voltage was varied, a transition from Cr_2O_3 to Al_2O_3 was observed, which was attributed to the breaking of Cr–O bonds due to ion bombardment and the lower enthalpy of formation of aluminium oxide compared to Cr_2O_3. Furthermore, a transition from incoherent to semi-coherent interfaces was observed as the bias voltage increased from 0 V to −50 V.

Nonetheless, there is limited literature that quantifies adhesion strength and interface chemistry, particularly for films fabricated on steel substrates. In this context, we focus on the widely studied CoCrFeNi HEA, known for its promising bulk properties [27]. Given EN-24′s broad applications in gears, shafts, and structural elements, it is crucial to develop hard films with improved adhesion to enhance the overall performance. Also, based on the previous studies, it is suggested that varying substrate temperatures [31,33] can improve film properties, likely due to the enhanced ad-atomic mobility [34], which may also modify the interface chemistry and improve the adhesion.

In the current study, non-equiatomic CoCrFeNi thin films were fabricated on EN-24 alloy steel substrates using direct current (DC) magnetron sputtering at different substrate temperatures (RT, 200 °C, 300 °C, and 400 °C). The goal was to produce films with improved mechanical properties and better substrate adhesion. For this a combination of low deposition power and sufficient time for diffusion was chosen. While low deposition power increases fabrication time and allows atoms to diffuse more effectively, resulting in improved adhesion. The findings demonstrate how substrate temperature affects the films' surface chemistry, which in turn influences both their mechanical properties and adhesion strength.

This research addresses the gap in literature regarding interface chemistry modification for improved adhesion of hard HEA thin films. It represents a systematic investigation towards the study the effect of substrate temperature on both surface and interface chemistry, contributing to the development of films with enhanced mechanical properties and excellent adhesion, suitable for protective coatings in various engineering applications.

2. Experimental procedure

2.1. Substrate preparation

The EN-24 alloy steel (~ 1.5 Ni, 1 Cr, 0.2 Mo, 0.9 C and Bal. Fe (wt. %)) was used as the substrate material for the thin film fabrication. The steel bulk were cut into several blocks of 30 mm × 30 mm × 5 mm in size. The pieces were then polished using SiC grinding papers up to 4000 grit size and subsequently with silica suspension (0.05 μm). The polished steel pieces were cleaned with deionised water and subsequently dried. The surface of the substrates was smooth and flat with no scratches when observed under the optical microscope. No further surface treatment was performed on the substrate prior to deposition.

2.2. Characterization of CoCrFeNi thin-film coatings

Non equi-atomic CoCrFeNi high entropy alloy thin films were deposited on the polished steel substrates using the direct current (DC) magnetron sputter deposition system (Make: M/s Excel instruments, Mumbai, India). For this purpose, disc type HEA composite target of $Co_{0.25}Cr_{0.25}Fe_{0.25}Ni_{0.25}$ target, with 50 mm diameter, 3 mm thickness and 99.99 % purity, were utilized. The sputtering chamber was first pumped to a base pressure (~ 1.3×10^{-5} Pa) using a combination of turbomolecular and rotary pumps. To spark the plasma, argon gas was

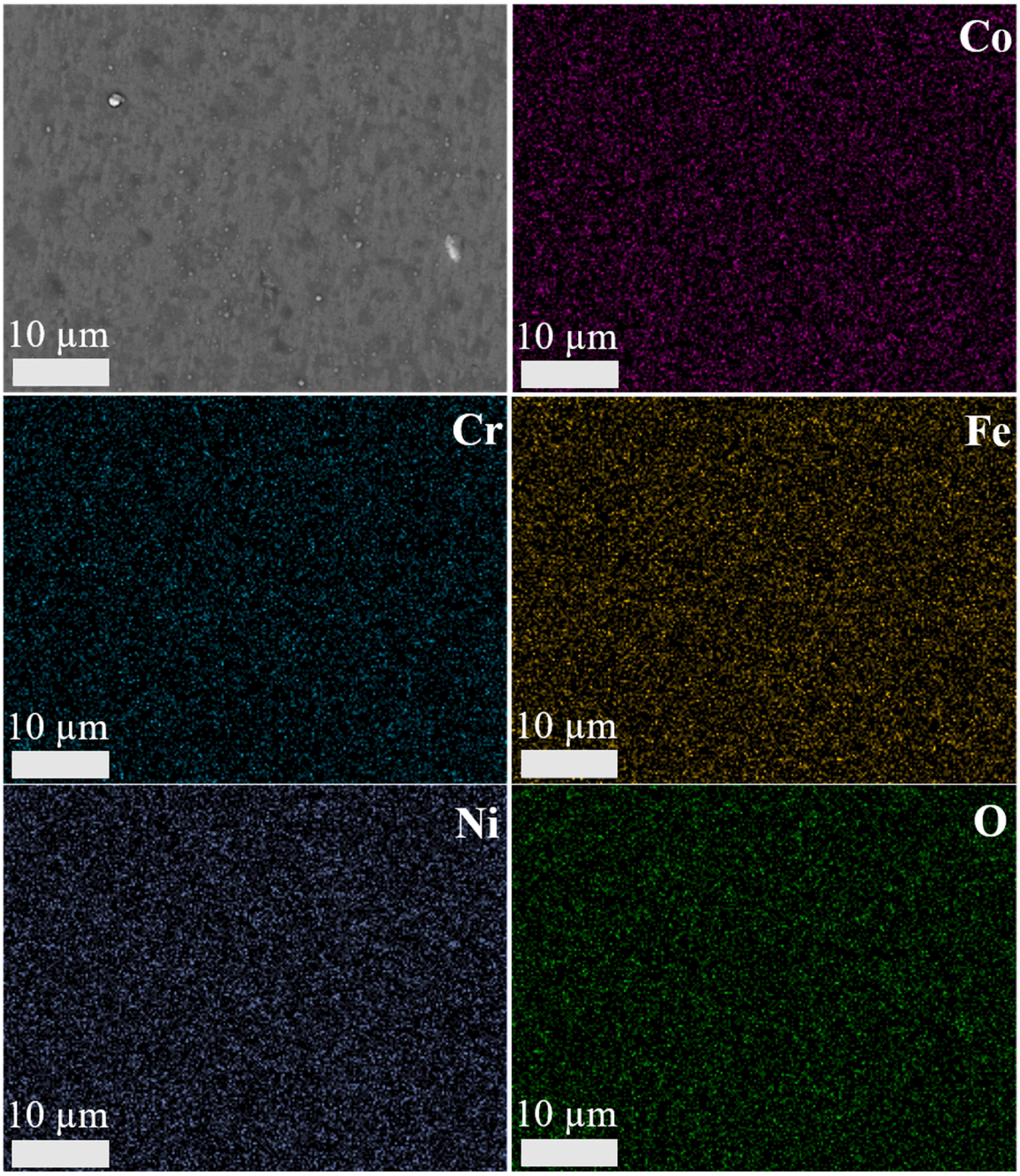

Fig. 2. EDS maps of CoCrFeNi thin film deposited at room temperature. The corresponding secondary electron image and the colour maps of individual elements are shown (observed along surface-normal direction).

supplied in a sputtering chamber at a flow rate of 15 sccm at working pressure of 0.15 Pa. The deposition was done with substrate-target distance of 15 cm at 45 ° substrate-target orientation. For estimating the deposition rate, the CoCrFeNi film was first deposited on a silicon (100) single-crystal substrate at a sputtering power of 20 W. The growth rate was found to be 2.6 nm/min, estimated using X-ray reflectivity (XRR) measurements. Based on this, the deposition was performed for 5 h 46 min to achieve the desired 0.9 μm thick CoCrFeNi film on EN-24 steel substrate. During deposition, the substrate assembly was rotated at around 2.5 RPM to achieve a uniform film. The film was fabricated at Room Temperature (~ 25 °C), 200 °C, 300 °C and 400 °C. The heating rate was 14–15 °C/min, with a 30-minute holding time to achieve temperature stability.

The growth morphology and the thickness of the film were examined using scanning electron microscopy (SEM) (JEOL 7800F) in secondary electron imaging mode and EDS at 15 keV voltage. To prepare the cross-sectional view of the film, mechanical polishing was performed at the edge of the sample using 4000-grit SiC paper under minimal pressure. Due to the extended deposition time, the film exhibited lateral diffusion and overgrowth beyond the substrate edges, which made it difficult to observe the film morphology in its as-deposited condition. Thus, localized polishing was employed at the edges of the sample which allows a slight chip-off of the film and thereby permitting imaging of the cross-section of the film. The elemental compositions of the films were evaluated using an energy dispersive spectroscopy (EDS) detector attached to a tabletop HITACHI TM3000 SEM at 15 keV voltage in surface-normal direction.

X-ray diffraction (XRD) and XRR measurements were performed to

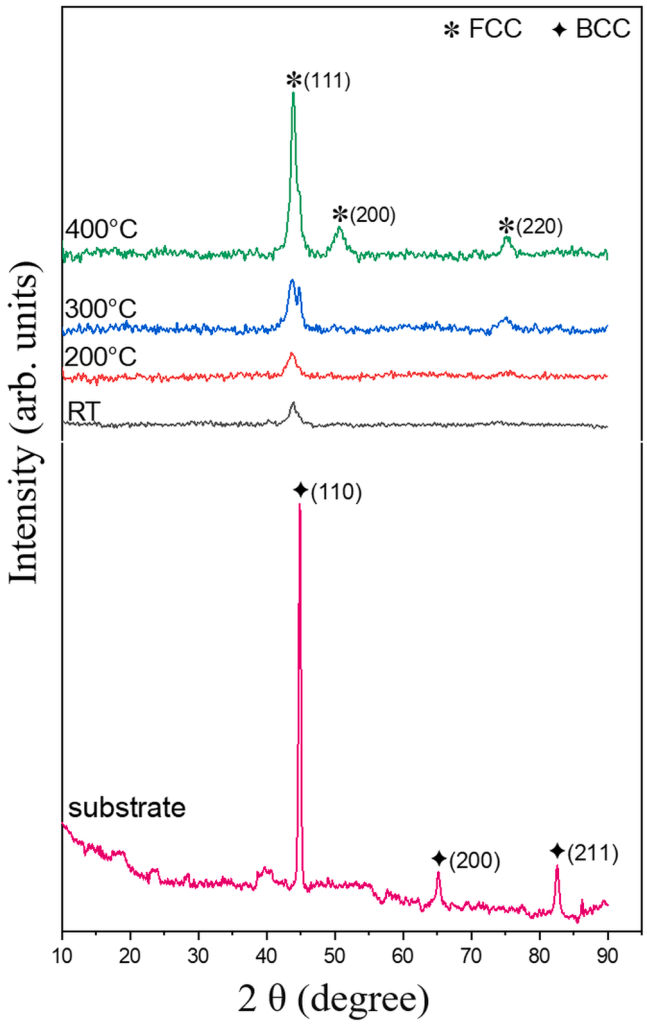

Fig. 3. GI-XRD patterns from CoCrFeNi HEA thin films deposited at substrate temperatures of RT, 200 °C, 300 °C, 400 °C along with Gonio XRD pattern of un-coated bare EN-24 substrate.

Table 1
Energy dispersive spectroscopy (EDS) elemental composition (in at. %) of the CoCrFeNi HEA thin film deposited at various substrate temperatures (observed in surface-normal direction).

Element	RT	200 °C	300 °C	400 °C
Co	22	22	22	22
Cr	19	19	19	19
Fe	23	23	24	23
Ni	23	22	23	23
O	11	11	10	11

estimate the structural quality and deposition rate of films using a Malvern PAN analytical manufactured X-ray diffractometer (Model: *X'pert3*) equipped with Cu-K_α X-ray source ($\lambda = 1.5406$ Å). The XRD measurements were performed in glancing incidence XRD (GIXRD) mode at an incident angle $\omega = 1.5°$.

The crystallite size of the CoCrFeNi thin films was calculated using the Debye-Scherrer equation:

$$D = \frac{k\lambda}{\beta\cos\theta} \quad (1)$$

where k is the shape factor (0.9), λ is the wavelength of the CuKα X-rays (1.541 Å), β is the full-width half maximum and θ is the Bragg angle

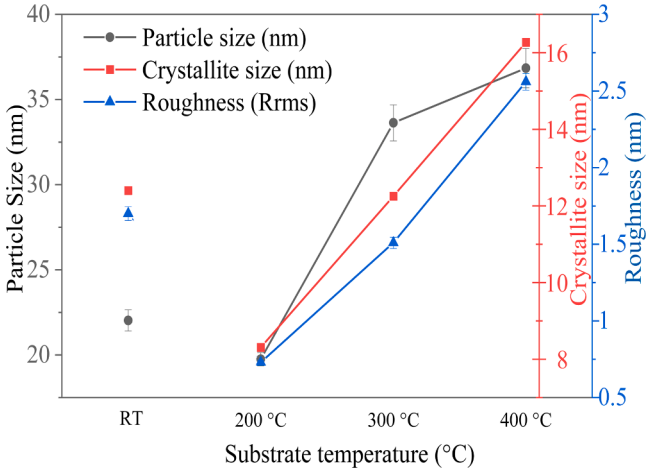

Fig. 4. Variation in particle size, crystallite size and surface roughness of the CoCrFeNi HEA films as a function of substrate temperature (the error bars here represent the standard deviation for the measured values of particle size, crystallite size and the surface roughness. The data points for RT are not connected intentionally to the 200 °C data points, as no direct comparison is intended. However, the points for 200 °C, 300 °C, and 400 °C have been joined to visually indicate the trend within the controlled temperature series.).

[35].

An atomic force microscope (AFM, Flex Axiom, and Drive AFM, Nanosurf, Switzerland) was used to measure the surface roughness and the particle size. This was carried out in the contact mode with a scan area of 1 μm × 1 μm. Gwyddion 2.60 software was used to analyze the surface roughness and ImageJ software was used to measure the particle size.

Nanoindentation (Hysitron/Bruker TI 750) tests were carried out using a Berkovich tip of radius 100 nm. A maximum load of 5 mN, 0.2 mN/s loading and unloading rate and 10 s dwell time at the maximum load was used. It was ensured that the maximum indentation depth remained within 1/10th of the thickness of the film to eliminate any effect of the substrate on the measurements. A total of 15 indents were made at different locations and the average values of hardness and modulus were reported. The hardness (H) and elastic modulus are calculated using the Oliver-Pharr formula [36]

$$H = \frac{P_{max}}{A} \quad (2)$$

where A is the contact area between the indenter and the specimen,

The elastic modulus of the film (E_s) can be calculated from the reduced modulus (E_r) [36] as given below:

$$\frac{1}{E_r} = \frac{1-\nu_i^2}{E_i} + \frac{1-\nu_s^2}{E_s} \quad (3)$$

where ν_s and E_s is the Poisson's ratio and Modulus of the specimen (film in this case), E_i and ν_i are the Young's modulus and Poisson's ratio of the diamond indenter, respectively. It is reported that E_i and ν_i are 1140 GPa and 0.07 [37]. Furthermore, ν_s of CoCrFeNi was taken to be 0.25 [38].

The incremental load scratch tests were performed on ASMEC's Universal Nanomechanical Tester (Bautzner Landstraβe 45, Germany) using a diamond cono-spherical tip of radius 10 μm. Indentation scratches under incremental load conditions were used to determine the critical load for delamination/failure of the film. The critical loads for crack initiation (Lc_1) and complete delamination (Lc_2) were estimated as per ASTM C1624–05 [39].

With the main objective to penetrate through the film and reach the bulk beneath. The scratch length, load, and scratching speed were carefully selected to ensure better resolution in terms of quantifying the critical load within the instrument's limitations This was done over a

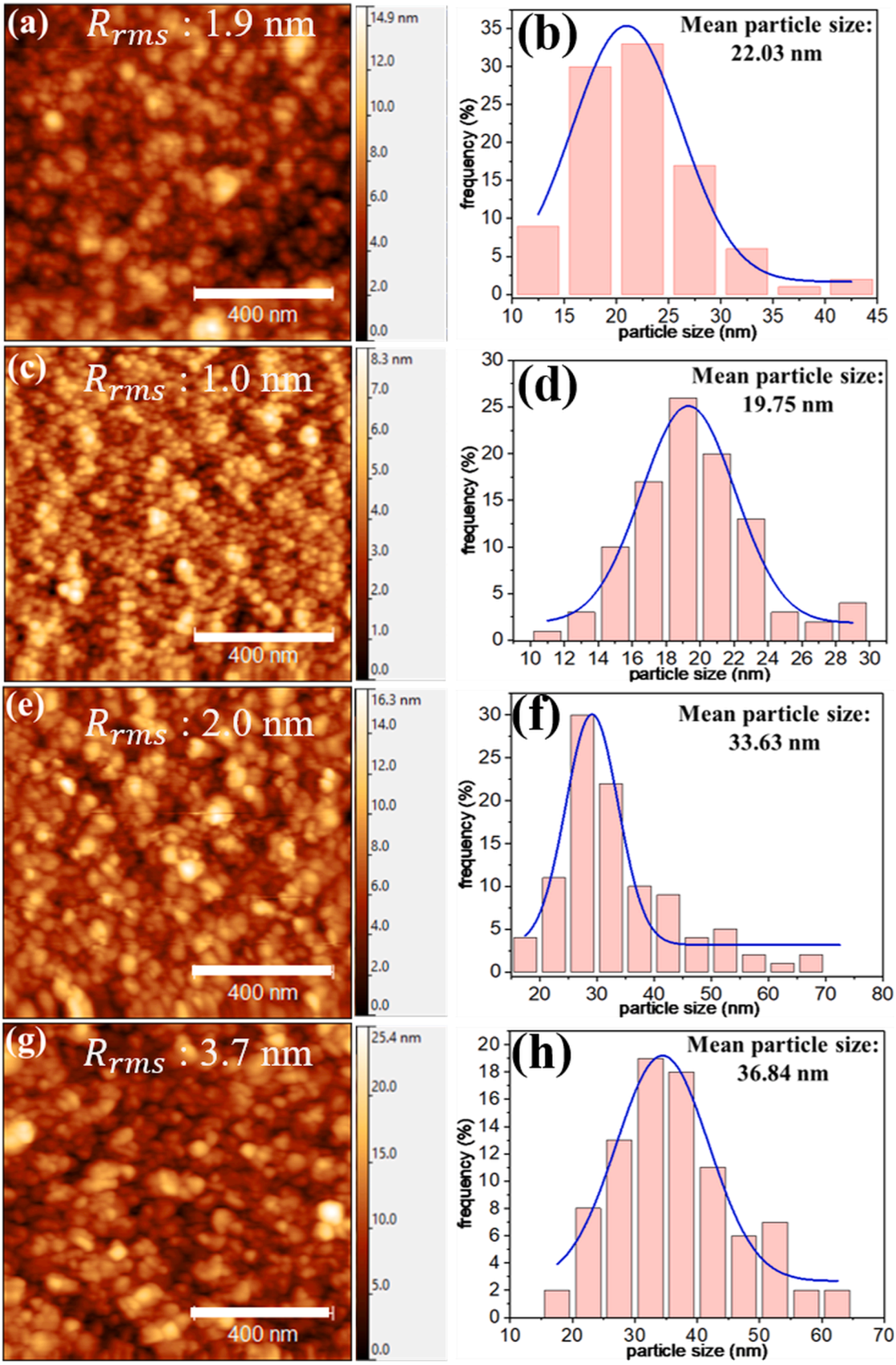

Fig. 5. Two-dimensional AFM images (the corresponding root mean square roughness values of the films are mentioned inside the concerning micrographs) along with a statistical histogram of particle size for CoCrFeNi HEA thin films deposited at various substrate temperatures of (a, b) RT, (c, d) 200 °C, (e, f) 300 °C and (g, h) 400 °C..

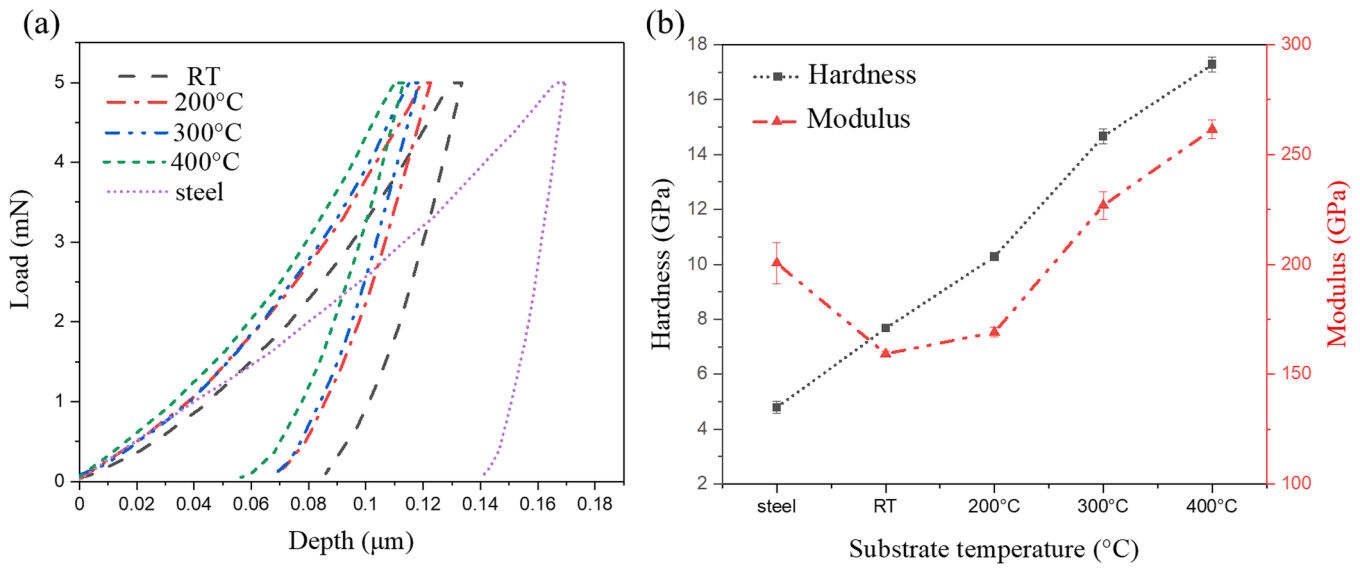

Fig. 6. Nanoindentation (a) load-displacement (P-h) curves and (b) corresponding hardness (H) and modulus (E) of CoCrFeNi thin films deposited at different substrate temperatures (error bars in Figure (b) represent the standard deviation of the hardness and modulus values).

scratch length of 250 μm under increasing load from 1–250 mN at 5 μm/s scratch speed. A total of three scratches were performed in each case to ensure the repeatability.

After preparation of lamellae using focused ion beam scanning electron microscopy (FIB-SEM, Helios 5 Laser Hydra [Tri-Beam] System), transmission electron microscope (TEM) and scanning transmission electron microscope (STEM) (Talos F200X G2 S/TEM) analysis was performed, incorporating energy dispersive x-ray spectroscopy (EDS) mapping and line-scans. The lamellae were approximately 20 μm x 10 μm, thinned using a 30 kV xenon ion beam to a thickness of near 200 nm. This was polished with a lower voltage (0.5 kV - 5 kV) xenon or argon ion beam to remove irradiation damage caused through the high voltage ion beam. The TEM and STEM-EDS data were taken with the sample surfaces and protective platinum coating oriented vertically, ensuring that the line-scans provided depth-based data leading to accurate coating thickness measurements.

3. Results and discussion

3.1. Thin-film characterisation

Fig. 1 shows cross-sectional views of HEA thin films deposited onto EN-24 steel substrates at RT, 200 °C, 300 °C, and 400 °C. The thickness of films are 883 ± 2 nm, 871 ± 2 nm, 915 ± 10 nm, and 905 ± 6 nm for substrate temperatures of RT, 200 °C, 300 °C and 400 °C, respectively. Moreover, it can be noticed that the films exhibit a columnar grain structure (also confirmed by the TEM results presented later).

The EDS elemental distribution map obtained from the top surface of a representative film is presented in Fig. 2. The elemental maps indicate a uniform distribution of the individual elements without any visible segregation also supported by STEM- elemental analysis (Fig. 9). This uniformity, combined with the XRD results (shown in Fig. 3) showing the absence of any additional diffraction peaks confirm the formation of the single-phase solid solution. Table 1 shows the corresponding quantitative analysis of various elements. It has been observed that the atomic percentages of all elements remained consistent with varying substrate temperatures showing no significant compositional changes. This observation is further supported by cross-sectional STEM maps (Fig. 9) and cross-sectional EDS line profile (Fig. 10), which will be discussed in detail later. Therefore, the impact of substrate temperature on the film composition is considered negligible. However, the presence of Oxygen and its effects are discussed in later sections of the paper.

Fig. 3 displays typical Grazing incidence X-Ray diffraction patterns of CoCrFeNi HEA thin films deposited at RT, 200 °C, 300 °C and 400 °C. A single common peak is observed at $2\theta = 43.71°$ for the all the fabricated films. This is in good agreement with the (111) plane of the single-phase FCC in CoCrFeNi HEA [19,40,41]. The peaks that appear on the GI-XRD patterns of films fabricated were matched with all the possible peaks in the binary phase diagram of each pair of elements in the HEA and the reported phases in the bulk CoCrFeNi HEA. The analysis confirmed that the peaks HCP-Co [42], FCC—Ni [42], Rhombohedral-Cr_2O_3 [43] possible cubic intermetallic of $FeNi_3$ [44], BCC—Cr [35] and Tetragonal σ-phase [45] did not match with the peaks of CoCrFeNi [19,40,41] further confirming the formation of single phase solid solution of FCC.

The broadening of the peaks visible for X-ray diffraction patterns for RT and 200 °C is attributed to the smaller crystallite sizes [31] and as the substrate temperature increased, there is a reduction in the broadness of the {111} peaks with increased intensity signifying the grain growth in preferred orientation. In addition, peaks corresponding to {200} and {220} planes also appear at higher substrate temperatures which according to Pelleg et al. [46] and Gao et al. [47], is attributed to the film's tendency to minimize its total energy- a combination of surface and strain energy during its growth. At lower substrate temperatures where ad-atomic mobility is lower, crystals with an FCC structure tend to grow along the (111) plane because this results in the lowest surface energy, which helps maintain stability. However, with an increase in temperature, the XRD spectrum exhibits a strong {111} and weak {200} and {220} reflections at $2\theta = 43.71°$, 50.73° and 75.67°, respectively. This is attributed to the increased ad-atomic mobility which favours the growth of the film in {200} and {220} directions. Moreover, the crystallite size is calculated via Debye-scherrer formula [35] and can be seen in Fig. 4.

Fig. 4 provides a summary of variation in particle size, crystallite size and roughness as a function of substrate temperature while the corresponding AFM images that show the two-dimensional and three-dimensional micrographs along with their statistical histograms are shown in Fig. 5. Particle size here refers to the overall dimensions of the surface features or grains observed (as seen in AFM micrographs, Fig. 5) which may consist of one or more crystallites. In contrast, crystallite size refers to the coherent diffracting domains within the material [48] -that is, regions over which the crystal lattice is continuous and free from defects or grain boundaries (as estimated from the X-ray diffraction patterns using the Scherrer equation [35]). The crystallite size increased from approximately 8 nm at 200 °C to 16 nm at 400 °C. The surface roughness exhibited a similar trend, increasing with particle size and

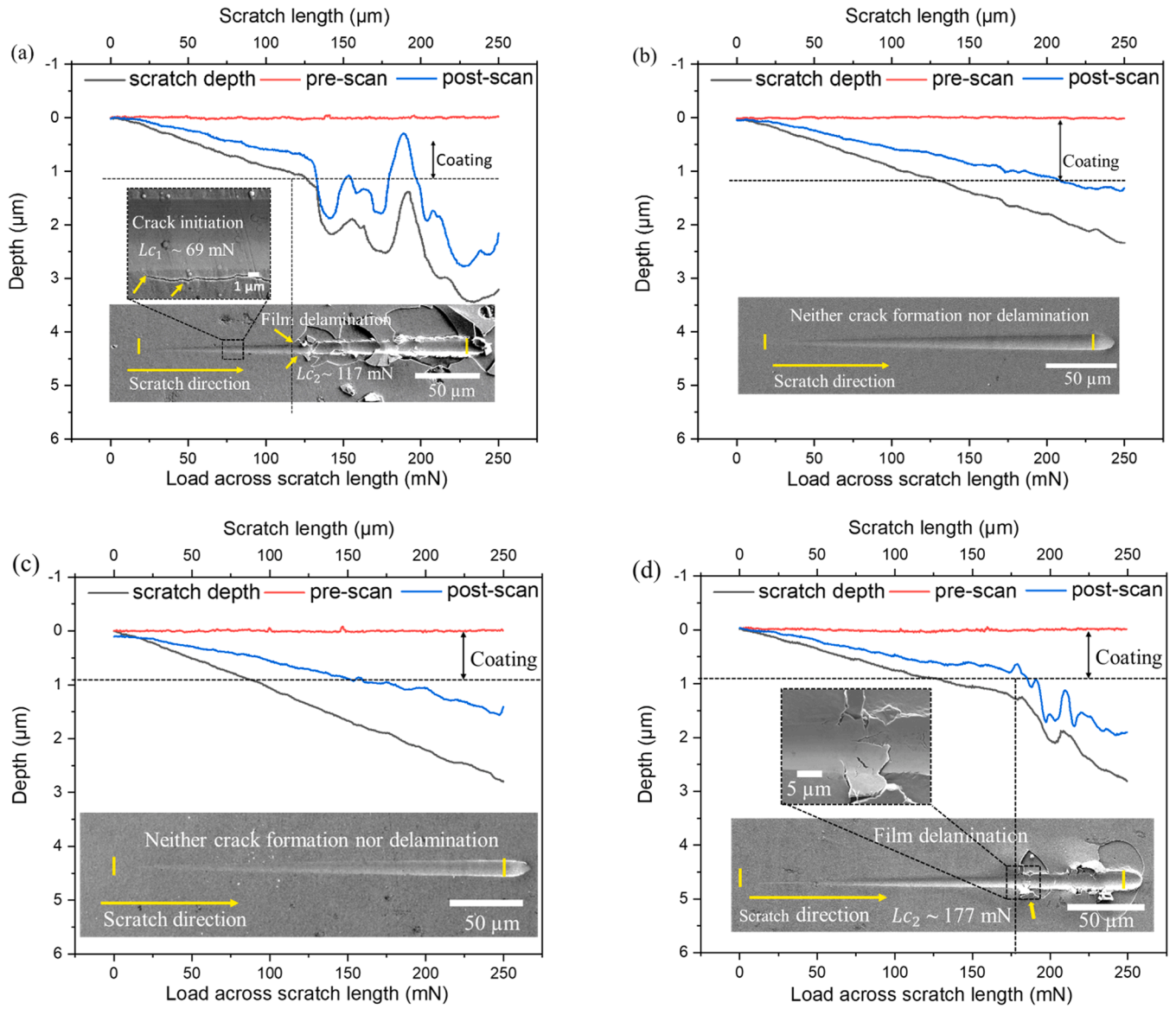

Fig. 7. Increasing load scratch profiles on films deposited at substrate temperature (a) RT, (b) 200 °C, (c) 300 °C and (d) 400 °C. The long yellow arrow represents the scratch direction (Lc_1 and Lc_2 here represent the critical load for crack initiation and critical load for delamination respectively).

reaching a maximum of 3.75 nm at 400 °C. Meanwhile, the mean particle size remained relatively stable at RT (~ 22 nm) and 200 °C (~ 20 nm), before increasing significantly to ~36 nm at 400 °C.

Here, the microstructural evolution corresponding to these fabricated films can be well explained by structure zone models (SZM) proposed by Thornton [49] which mainly consists of 3 zones and are a function of homologous temperature ($\theta = T_s / T_m$) with unique features primarily influenced by processing parameters [50]. In the Zone 1, where the temperature is relatively low, the growth is predominantly governed by shadowing effect [33,34] with limited adatom mobility. These conditions result in a columnar structure with reduced grain dimensions. However, in Zone 2, as the substrate temperature increases, surface diffusion [34] becomes the primary mechanism influencing the film growth. Though the columnar structure persists in Zone 2, the enhanced adatom mobility facilitates the formation of larger particle and a denser columnar structure [34].

The films fabricated at room temperature (RT) and 200 °C here exhibit microstructural features similar to Zone 1 of the SZM as evidenced by the columnar morphology observed in the cross-sectional SEM images (Fig. 1). Additionally, the broadening of the X-ray diffraction (XRD) peaks at these temperatures (Fig. 3, for RT and 200 °C) indicates a reduction in crystallite size and poor crystallinity [29,34], which is consistent with limited adatom diffusion under low-temperature conditions. Furthermore, atomic force microscopy (AFM) analysis reveals smaller particle sizes and fine surface features for films deposited at RT and 200 °C (Fig. 4), further supporting the inference of restricted adatom mobility. The observed poor crystallinity and limited particle coalescence can thus be attributed to the insufficient surface diffusion, aligning well with the predictions of Zone 1 behaviour in the SZM framework.

Moreover, the films fabricated at 300 °C and 400 °C also exhibited columnar structures, as confirmed by fractured cross-sectional SEM images (Fig. 1) and cross-sectional TEM bright-field images (Fig. 9). XRD analysis (Fig. 3) indicates improved crystallinity [29,34] at these temperatures, consistent with enhanced adatom mobility. Additionally, AFM measurements (Figs. 4 and 5) show an increase in particle size, further supporting the effect of elevated substrate temperatures on surface diffusion [34]. These microstructural and crystallographic features reflect the transition from Zone 1 to Zone 2 behaviour within the SZM, where increased thermal energy promotes adatom surface

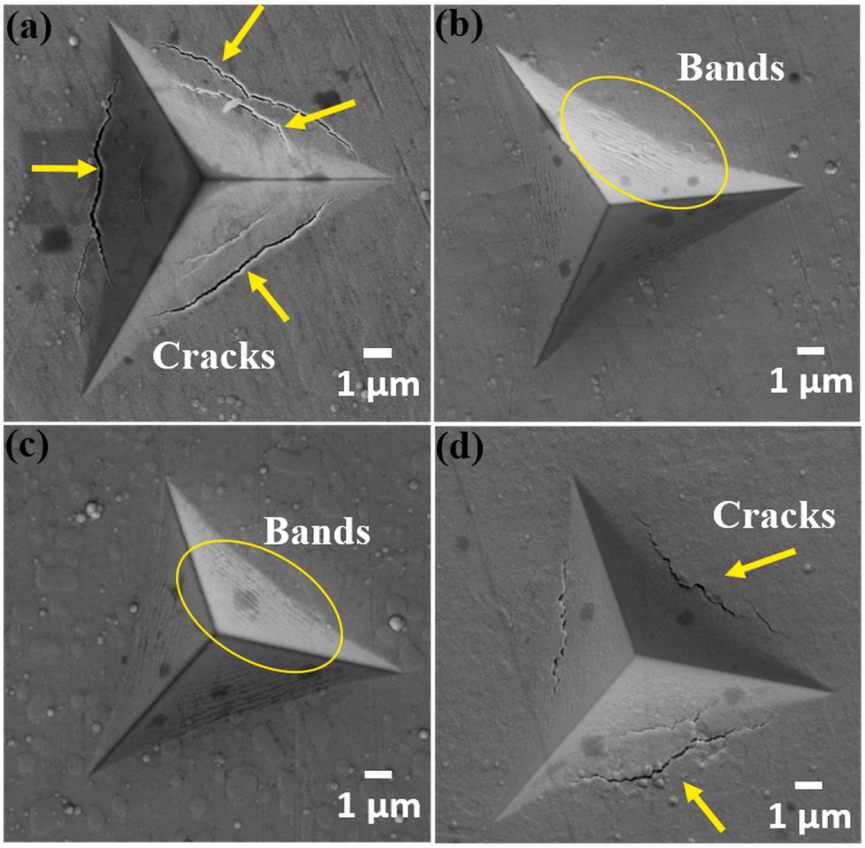

Fig. 8. The micrographs of the indents performed at 250 mN with varying substrate temperatures at (a) RT, (b) 200 °C, (c) 300 °C, and (d) 400 °C. The yellow arrows point towards the cracks, while the yellow ellipse shows the band-like structure formed post-indentation.

diffusion, leading to better crystallinity, larger particle size, and denser columnar growth [50].

3.2. Nano-mechanical tests

To investigate the effect of substrate temperature on the nano-mechanical properties of the thin films, including hardness (H) and Young's modulus (E), nanoindentation tests were performed on the film's top surface. Fig. 6(a) shows the typical load-displacement (P-h) curves of thin films deposited at different substrate temperatures. The corresponding hardness and modulus evolution are shown in Fig. 6(b). Note that both exhibit a similar trend of increase in value with increasing substrate temperature. The hardness and modulus of the films reach their peak values at 400 °C, measuring 17.28 ± 0.2 GPa and 261.5 ± 4 GPa, respectively. Notably, the hardness at this temperature is four times greater than that of the uncoated substrate (4.79 ± 0.2 GPa). While the increase in particle size may appear to contradict the conventional Hall-Petch relationship, such deviations are not uncommon in nanocrystalline thin films. Feng et al. [51] reported a similar discrepancy in Ni thin films, which possessed a FCC crystal structure. In their study, specific deposition conditions led to strong (111) preferential growth orientation and an associated increase in hardness, despite the presence of larger grains which aligns well with the results observed in this study. Therefore, the improved hardness for the film deposited at 400 °C can be attributed to combined effects of improved crystallinity, enhanced columnar density (explained by the SZM model [50]) and preferential orientation of the film.

Here, the modulus of RT and 200 °C film is observed to be lower than the conventional CoCrFeNi alloy (~ 226 GPa [52]). The elastic modulus of crystalline materials is inherently anisotropic and varies significantly with crystallographic orientation. Particularly, in FCC metals, the elastic modulus attains its maximum value along the ⟨111⟩ direction, owing to the dense atomic packing of the (111) planes, which result from stronger interatomic bonding and enhanced resistance to elastic deformation.

The lower modulus observed in the RT and 200 °C can be attributed to their weak preferential orientation, as indicated by the low intensity of the (111) peak in the XRD. However, the 300 °C and 400 °C films exhibited higher modulus values which can be rationalised to the stronger preferential orientation along (111) crystallographic plane. This enhanced alignment increases the contribution of the stiffer ⟨111⟩ direction to the overall elastic response, thereby accounting for the increased elastic modulus observed at these temperatures.

3.3. Adhesion strength of thin films

It is envisaged that good adhesion is required between the substrate and film interface to avoid delamination when the film is subjected to stress. The scratch adhesion strength is determined using the scratch test performed with incremental loading conditions. The scratch adhesion strength is determined as the critical load at which the film is delaminated (Lc_2).

The results show that the film deposited at RT is observed to delaminate at a critical load (Lc_2) of ~ 117 mN, although cracks started to initiate at a much lower load (Lc_1 – load at which the crack initiated) of ~ 69 mN as shown in Fig. 7(a). In contrast, the critical load (Lc_2 -load at which the film completely delaminated) for the film deposited at 400 °C was found to be much higher than that of the film deposited at RT which is ~180 mN (Fig. 7(d)). This can also be seen from the depth profiles extracted from the nanoindentation based scratch tests on the films deposited at various substrate temperatures (Fig. 7). Notably, the scratch depth for the films deposited at 200 °C and 300 °C has reached beyond the film thickness (~ 1 μm) (Figs. 7(b) and 7 (c)). Despite this,

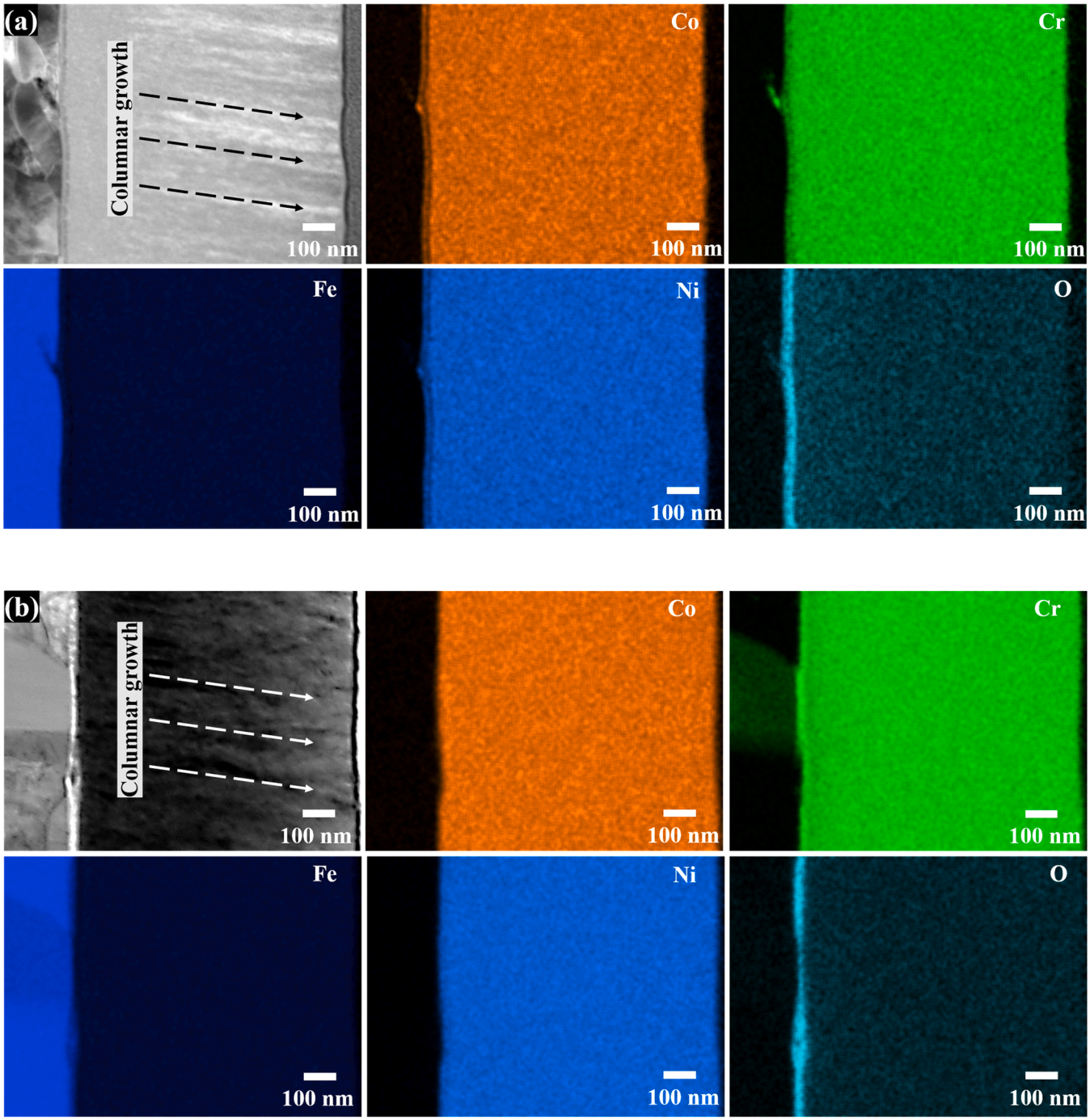

Fig. 9. Cross-sectional STEM elemental maps for films deposited at (a) 300 °C and (b) 400 °C. The elements are indicated at the top right corner of the map.

there is no evidence of delamination which suggests extremely good adhesion of the films to the substrate.

To further understand the fracture behavior of the film in static mode, a Quasi-continuous stiffness mode was used with a maximum load of 250 mN and Fig. 8 (a-d) shows micrographs of the indents corresponding to them. The films fabricated at RT and 400 °C showed brittle fracture, whereas the films deposited at 200 °C and 300 °C showed no evidence of fracture. For the latter case, the indentation mark appeared to show a band-like structure, as indicated by the yellow ellipse (Figs. 8(b) and (c)). These are likely formed due to localized plastic deformation in the film under applied load. During indentation, the stress field beneath the indenter induces slip and shear band formation [53], which appeared here as band-like features on the film surface. Their presence, without signs of interfacial delamination or spallation, indicates that the applied stresses were accommodated by the film without causing failure. Therefore, these results combined with the scratch results confirm the excellent adhesion of the substrate-film in the case of the films deposited at 200 °C and 300 °C.

The $\frac{H}{E}$ ratio, recognised as an indicator of material toughness [54], suggests that, lower values correspond to reduced toughness and vice versa. Here, in the film deposited at room temperature (RT), the primary cracks observed in Fig. 8(a) correspond to the crack initiation load (~ 69 mN) attributed to the films lowest $\frac{H}{E}$ ratio (0.04811), reflecting its poor toughness, while the secondary cracks indicate the critical load for delamination. Although, the film fabricated at 400 °C is observed to have maximum $\frac{H}{E}$ ratio (0.0660) the cracks observed in the Fig. 8. (d)

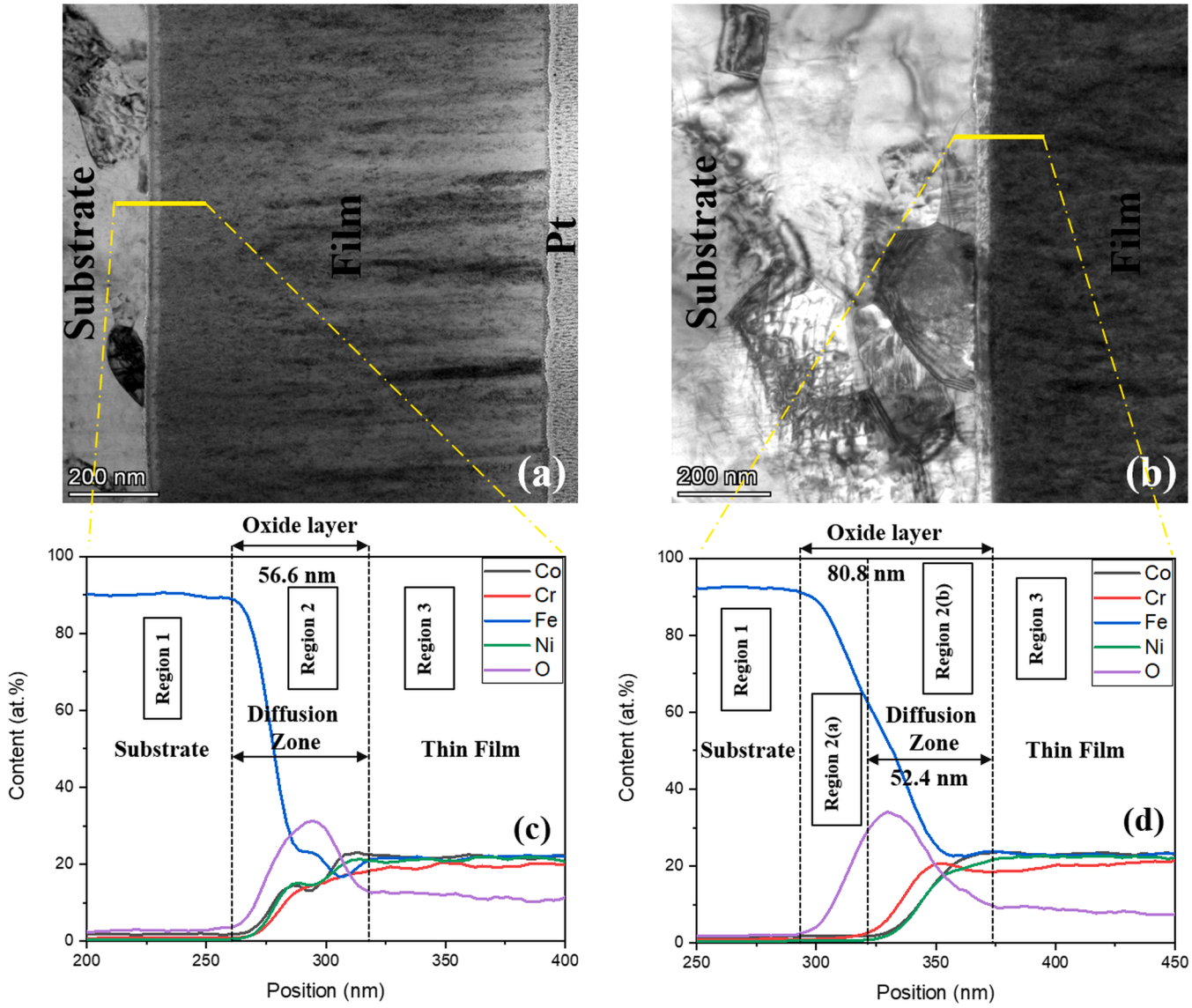

Fig. 10. Bright field imaging and the corresponding STEM-EDS line profiles across the interface for (a, c) 300 °C and (b, d) 400 °C.

correspond to the critical load for delamination. This behaviour is further discussed in later sections, particularly in the context of interfacial chemistry revealed through cross-sectional analysis.

3.4. Cross-sectional analysis of thin films

To further understand the governing factors for adhesion, a section of the film is ion-milled using FIB and observed under TEM. The samples fabricated at room temperature (RT) and 200 °C were excluded from characterization, focussing on analysing each delaminated (400 °C) and non-delaminated (300 °C) cases. This should provide sufficient insights into the factors influencing interface bonding and delamination. Fig. 9 shows TEM-bright field images of two cross-sectional FIB-lamellae along with their STEM elemental maps. The bright field images (Fig. 9(a) and (b)) clearly reveal the columnar structure of the fabricated thin films. The thickness of the films measured from the below TEM micrographs are 899 ± 3 nm and 870 ± 3 nm which are also consistent with the thickness measured from SEM micrographs with no significant variation.

TEM images of selected conditions are shown in Fig. 10 along with their elemental concentration line profiles. Based on the oxygen elemental maps in Fig. 9 and the oxygen hump (region 2 in Fig. 10(c) and (d)) visible within dashed lines in the STEM-EDS elemental line profile (purple colour line profile, Fig. 10(c) & (d)), it confirms the formation of a dense oxide layer at the film-substrate interface. The evolution of the oxide at the interface at these temperatures is attributed to the naturally occuring FeO_x [55]and CrO_x [56] on the steel substrate after the sample polishing and prior to sputtering. This is evident from the concentration profiles (blue and purple) in Region 2(a) of Fig. 10, indicating the presence of FeO_x, consistent with the STEM elemental maps shown in Fig. 9. Additionally, the Cr elemental line profile in Figure 10(d) in Region 2 (b). shows a higher concentration near the oxygen hump compared to other elements, suggesting the presence of minor fractions of CrO_x. However, in the case of film deposited at 300 °C, although the oxide profiles are less distinct, the presence of interfacial oxides is still considered likely-supported by the clear oxide formation at 400 °C and also being consistent with the findings of Zhao et al. [32]., which reports such naturally oxide formation are unavoidable.

Although, the width of the oxygen line profile that depict the thickness of the oxide layer were observed to be ~ 57 nm for 300 °C film and ~ 81 nm for 400 °C film. This increase here is predominantly due to the variation in time taken to attain the working temperature. The time taken here for the substrate to attain 300 °C was ~ 50 mins (15 °C/min

heating rate + 30 mins holding to attain stability) and for 400 °C it was ~ 58 mins (15 °C/min heating rate + 30 mins holding to attain stability) during which the oxide layer is grown owing to the increased oxidation kinetics [57,58] which promote faster growth of oxide layer. In the current work, it is possible that some residual oxygen may emanate owing to the use of turbo-molecular pump. This has been confirmed from the residual gas analysis (see Figure S5) performed at base pressure (~ 10^{-4} Pa) that show the presence of oxygen with partial pressure of 2.2×10^{-5} Pa inside the vacuum chamber.

In Figures 10(c) and 10(d), Region 1 corresponds to the steel substrate, while Region 3 represents the thin film, with the elemental atomic percent distributions closely matching those obtained from the SEM-EDS analysis (Table 1). The variations in the atomic percent of Co, Cr, Fe, and Ni within Region 2 in both figures indicate a compositional gradient, suggesting that the process at the interface is governed by diffusion [59].

The atomic concentration profiles of Co, Cr, Fe, and Ni in Region 2 of Figure 10(c) indicate that diffusion extended up to the onset of the oxide hump on the substrate side. This suggests the formation of a diffusion bond at the interface, comprising a mixture of oxides and HEA alloying elements. Such interfacial chemistry can be attributed to the excellent adhesion observed in the film fabricated at 300 °C, which exhibited neither delamination nor cracking during scratch testing.

In contrast, for the film deposited at 400 °C, diffusion appears to be limited to a narrower region (as seen in region 2 (b) in Fig. 10(d)) leaving a thin FeO_x interlayer (~30 nm) intact (as seen in region 2 (a) of Fig. 10(d)). This incomplete diffusion, along with the presence of FeO_x and CrO_x at the interface, accounts for the reduced adhesion and delamination observed in the 400 °C film.

4. Conclusions

This research reports on the effects of substrate temperature on the film characteristics, mechanical properties, and adhesion strength of magnetron sputtered HEA thin films. Non-equiatomic CoCrFeNi HEA was deposited onto EN-24 steel substrates up to a 0.9 μm thick layer at four different substrate temperatures: room temperature (RT), 200 °C, 300 °C, and 400 °C. Based on XRD studies, all the films displayed single-phase FCC crystal structures with a preferred orientation of (111). AFM analysis revealed that particle size and surface roughness increased with substrate temperature, reaching their highest values at 400 °C. The film deposited at 400 °C exhibited the highest modulus (~261 GPa) and hardness (~17 GPa). In terms of adhesion, the critical load for delamination (LC_2) was approximately 180 mN for the 400 °C film and 120 mN for the room temperature (RT) film. However, films deposited at 200 °C and 300 °C showed no signs of delamination, indicating strong interfacial adhesion between the substrate and film. The delamination observed in the 400 °C film is attributed to limited diffusion across a thicker oxide layer, whereas the 300 °C film demonstrated exceptional adhesion due to the formation of a diffusion bond with the substrate.

In conclusion, substrate temperature significantly influences the mechanical and adhesion properties of the films. Optimizing the combination of sputtering power and substrate temperature is essential to achieve desirable film characteristics. In our study, a setting of 20 W sputtering power and 300 °C substrate temperature showed great promise for applications requiring high adhesion, hardness, and modulus.

CRediT authorship contribution statement

M. Subhakar: Writing – review & editing, Writing – original draft, Methodology, Investigation, Data curation, Conceptualization. **L. Pandey:** Investigation. **S. Chaudhary:** Writing – review & editing, Resources. **S.P. Jaiswal:** Investigation. **S.S. Singh:** Writing – review & editing, Resources. **U. Mahmud:** Investigation. **Y.L. Chiu:** Writing – review & editing, Resources. **I.P. Jones:** Writing – review & editing, Resources. **J. Jain:** Writing – review & editing, Supervision, Resources, Project administration, Funding acquisition, Conceptualization.

Declaration of competing interest

The authors declare that they have no known competing financial interests or personal relationships that could have appeared to influence the work reported in this paper.

Data availability

Data will be made available on request.

References

[1] S.S. Sohn, A. Kwiatkowski Da Silva, Y. Ikeda, F. Körmann, W. Lu, W.S. Choi, B. Gault, D. Ponge, J. Neugebauer, D. Raabe, Ultrastrong medium-entropy single-phase alloys designed via severe lattice distortion, Adv. Mater. 31 (2019) 1807142, https://doi.org/10.1002/adma.201807142.
[2] J.-W. Yeh, S.-K. Chen, S.-J. Lin, J.-Y. Gan, T.-S. Chin, T.-T. Shun, C.-H. Tsau, S.-Y. Chang, Nanostructured high-entropy alloys with multiple principal elements: novel alloy design concepts and outcomes, (2004). https://doi.org/10.1002/adem.200300567.
[3] B. Cantor, I.T.H. Chang, P. Knight, A.J.B. Vincent, Microstructural development in equiatomic multicomponent alloys, Mater. Sci. Eng.: A 375–377 (2004) 213–218, https://doi.org/10.1016/j.msea.2003.10.257.
[4] S. Guo, C. Ng, J. Lu, C.T. Liu, Effect of valence electron concentration on stability of fcc or bcc phase in high entropy alloys, J. Appl. Phys. 109 (2011) 103505, https://doi.org/10.1063/1.3587228.
[5] O.N. Senkov, G.B. Wilks, J.M. Scott, D.B. Miracle, Mechanical properties of Nb25Mo25Ta25W25 and V20Nb20Mo20Ta20W20 refractory high entropy alloys, Intermetallics 19 (2011) 698–706, https://doi.org/10.1016/j.intermet.2011.01.004.
[6] J. Luo, N. Zhou, High-entropy grain boundaries, Commun. Mater. 4 (2023) 7, https://doi.org/10.1038/s43246-023-00335-w.
[7] O.N. Senkov, C.F. Woodward, Microstructure and properties of a refractory NbCrMo0.5Ta0.5TiZr alloy, Mater. Sci. Eng.: A 529 (2011) 311–320, https://doi.org/10.1016/j.msea.2011.09.033.
[8] O.N. Senkov, S.V. Senkova, C. Woodward, Effect of aluminum on the microstructure and properties of two refractory high-entropy alloys, Acta Mater. 68 (2014) 214–228, https://doi.org/10.1016/j.actamat.2014.01.029.
[9] O.N. Senkov, S.V. Senkova, D.B. Miracle, C. Woodward, Mechanical properties of low-density, refractory multi-principal element alloys of the Cr–Nb–Ti–V–Zr system, Mater. Sci. Eng.: A 565 (2013) 51–62, https://doi.org/10.1016/j.msea.2012.12.018.
[10] A.V. Kuznetsov, D.G. Shaysultanov, N.D. Stepanov, G.A. Salishchev, O.N. Senkov, Tensile properties of an AlCrCuNiFeCo high-entropy alloy in as-cast and wrought conditions, Mater. Sci. Eng.: A 533 (2012) 107–118, https://doi.org/10.1016/j.msea.2011.11.045.
[11] Z. Tang, T. Yuan, C.-W. Tsai, J.-W. Yeh, C.D. Lundin, P.K. Liaw, Fatigue behavior of a wrought Al0.5CoCrCuFeNi two-phase high-entropy alloy, Acta Mater. 99 (2015) 247–258, https://doi.org/10.1016/j.actamat.2015.07.004.
[12] M. Seifi, D. Li, Z. Yong, P.K. Liaw, J.J. Lewandowski, Fracture toughness and fatigue crack growth behavior of As-cast high-entropy alloys, JOM 67 (2015) 2288–2295, https://doi.org/10.1007/s11837-015-1563-9.
[13] B. Gludovatz, A. Hohenwarter, D. Catoor, E.H. Chang, E.P. George, R.O. Ritchie, A fracture-resistant high-entropy alloy for cryogenic applications, Science 345 (2014) 1153–1158, https://doi.org/10.1126/science.1254581.
[14] Z. Lei, X. Liu, Y. Wu, H. Wang, S. Jiang, S. Wang, X. Hui, Y. Wu, B. Gault, P. Kontis, D. Raabe, L. Gu, Q. Zhang, H. Chen, H. Wang, J. Liu, K. An, Q. Zeng, T.-G. Nieh, Z. Lu, Enhanced strength and ductility in a high-entropy alloy via ordered oxygen complexes, Nature 563 (2018) 546–550, https://doi.org/10.1038/s41586-018-0685-y.
[15] S. Chen, Z.H. Aitken, S. Pattamatta, Z. Wu, Z.G. Yu, D.J. Srolovitz, P.K. Liaw, Y.-W. Zhang, Simultaneously enhancing the ultimate strength and ductility of high-entropy alloys via short-range ordering, Nat. Commun. 12 (2021) 4953, https://doi.org/10.1038/s41467-021-25264-5.
[16] D. Utt, S. Lee, Y. Xing, H. Jeong, A. Stukowski, S.H. Oh, G. Dehm, K. Albe, The origin of jerky dislocation motion in high-entropy alloys, Nat. Commun. 13 (2022) 4777, https://doi.org/10.1038/s41467-022-32134-1.
[17] W. Liao, S. Lan, L. Gao, H. Zhang, S. Xu, J. Song, X. Wang, Y. Lu, Nanocrystalline high-entropy alloy (CoCrFeNiAl0.3) thin-film coating by magnetron sputtering, Thin. Solid. Films. 638 (2017) 383–388, https://doi.org/10.1016/j.tsf.2017.08.006.
[18] N.G. Kipkirui, T.-T. Lin, R.S. Kiplangat, J.-W. Lee, S.-H. Chen, HiPIMS and RF magnetron sputtered Al0.5CoCrFeNi2Ti0.5 HEA thin-film coatings: synthesis and characterization, Surf. Coat. Technol. 449 (2022) 128988, https://doi.org/10.1016/j.surfcoat.2022.128988.
[19] J.-J. Wang, F.-Y. Ouyang, Nanotwinned medium entropy alloy CoCrFeNi thin films with ultra-high hardness: modifying residual stress without scarifying hardness through tuning substrate bias, Surf. Coat. Technol. 434 (2022) 128191, https://doi.org/10.1016/j.surfcoat.2022.128191.

[20] J.Y. Cheng, A. Hamilton, M. Odlyzko, M. De Leo, J.K. Baldwin, N.A. Mara, Thick graded interfaces increase wear resistance in Ti/TiN nanolayered thin films, Thin. Solid. Films. 816 (2025) 140653, https://doi.org/10.1016/j.tsf.2025.140653.
[21] Z. Tang, M.C. Gao, H. Diao, T. Yang, J. Liu, T. Zuo, Y. Zhang, Z. Lu, Y. Cheng, Y. Zhang, K.A. Dahmen, P.K. Liaw, T. Egami, Aluminum alloying effects on lattice types, microstructures, and mechanical behavior of high-entropy alloys systems, JOM 65 (2013) 1848–1858, https://doi.org/10.1007/s11837-013-0776-z.
[22] T. Yang, Y.L. Zhao, Y. Tong, Z.B. Jiao, J. Wei, J.X. Cai, X.D. Han, D. Chen, A. Hu, J. J. Kai, K. Lu, Y. Liu, C.T. Liu, Multicomponent intermetallic nanoparticles and superb mechanical behaviors of complex alloys, Science 362 (2018) 933–937, https://doi.org/10.1126/science.aas8815.
[23] C.K. Srivastav, N.S. Anuraag, A.K. Pandey, N.K. Prasad, D. Khan, Design, preparation and study of microstructure, phase evolution and thermal stability of Ti-Co0.35-Cr0.35-Nb-Zr nanocrystalline HEA for biomedical applications, Mater. Today Commun. 35 (2023) 105557, https://doi.org/10.1016/j.mtcomm.2023.105557.
[24] K.M. Döleker, Y. Özgürlük, O. Gokcekaya, A. Günen, A. Erdoğan, High-temperature corrosion and oxidation properties of borided CoCrFeNiAl0.5Nb0.5 HEA, Surf. Coat. Technol. 470 (2023) 129856, https://doi.org/10.1016/j.surfcoat.2023.129856.
[25] Y. Wang, X. Huang, Y. Liu, X. Zhang, B. Yang, Y. Yue, Thermal and mechanical characterization of under-2-μm-thick AlCrNbSiTi high-entropy thin film, Energy Storage Sav. 3 (2024) 52–59, https://doi.org/10.1016/j.enss.2023.06.002.
[26] W. Li, P. Liu, P.K. Liaw, Microstructures and properties of high-entropy alloy films and coatings: a review, Mater. Res. Lett. 6 (2018) 199–229, https://doi.org/10.1080/21663831.2018.1434248.
[27] J.-W. Yeh, Y.L. Chen, S.J. Lin, S.K. Chen, High-entropy alloys- A new era of exploitation, Mater. Sci. Forum Fam Plan West Hemisph 560 (2007), https://doi.org/10.4028/www.scientific.net/MSF.560.1.
[28] M. Liu, Y. Yang, Q. Mao, Y. Wei, Y. Li, N. Ma, H. Liu, X. Liu, Z. Huang, Influence of radio frequency magnetron sputtering parameters on the structure and performance of SiC films, Ceram. Int. 47 (2021) 24098–24105, https://doi.org/10.1016/j.ceramint.2021.05.120.
[29] N.A. Khan, B. Akhavan, C. Zhou, H. Zhou, L. Chang, Y. Wang, Y. Liu, L. Fu, M. M. Bilek, Z. Liu, RF magnetron sputtered AlCoCrCu0.5FeNi high entropy alloy (HEA) thin films with tuned microstructure and chemical composition, J. Alloys. Compd. 836 (2020) 155348, https://doi.org/10.1016/j.jallcom.2020.155348.
[30] K. Zhao, X. Hao, B. Huang, X. Zhao, J. Ma, C. Wang, Effect of bias voltage on the structure and properties of CoCrFeNi high entropy alloy thin films prepared by magnetron sputtering, Mater. Today Commun. 40 (2024) 110217, https://doi.org/10.1016/j.mtcomm.2024.110217.
[31] M. Hu, Q.P. Cao, X.D. Wang, D.X. Zhang, J.-Z. Jiang, Tuning nanostructure and mechanical property of Fe–Co–Ni–Cr–Mn high-entropy alloy thin films by substrate temperature, Mater. Today Nano 15 (2021) 100130, https://doi.org/10.1016/j.mtnano.2021.100130.
[32] H. Zhao, Z. Zheng, T. Jiang, L. Fu, B. Akhavan, M.M. Bilek, Z. Liu, High entropy alloy thin films on SS304 substrates: evolution of microstructure and interface modulated by energetic condensation in nanoscale, Mater. Mater Des 230 (2023) 111981, https://doi.org/10.1016/j.matdes.2023.111981.
[33] W. Yao, Q.P. Cao, S.Y. Liu, X.D. Wang, H.J. Fecht, A. Caron, D.X. Zhang, J.Z. Jiang, Tailoring nanostructured Ni-Nb metallic glassy thin films by substrate temperature, Acta Mater. 194 (2020) 13–26, https://doi.org/10.1016/j.actamat.2020.04.046.
[34] S. Mukherjee, D. Gall, Structure zone model for extreme shadowing conditions, Thin. Solid. Films. 527 (2013) 158–163, https://doi.org/10.1016/j.tsf.2012.11.007.
[35] A.L. Patterson, The Scherrer formula for X-ray particle size determination, Phys. Rev. 56 (1939) 978–982, https://doi.org/10.1103/PhysRev.56.978.
[36] W.C. Oliver, G.M. Pharr, An improved technique for determining hardness and elastic modulus using load and displacement sensing indentation experiments, J. Mater. Res. 7 (1992) 1564–1583, https://doi.org/10.1557/JMR.1992.1564.
[37] M. Mohr, A. Caron, P. Herbeck-Engel, R. Bennewitz, P. Gluche, K. Brühne, H.-J. Fecht, Young's modulus, fracture strength, and Poisson's ratio of nanocrystalline diamond films, J. Appl. Phys. 116 (2014) 124308, https://doi.org/10.1063/1.4896729.
[38] G. Laplanche, P. Gadaud, C. Bärsch, K. Demtröder, C. Reinhart, J. Schreuer, E. P. George, Elastic moduli and thermal expansion coefficients of medium-entropy subsystems of the CrMnFeCoNi high-entropy alloy, J. Alloys. Compd. 746 (2018) 244–255, https://doi.org/10.1016/j.jallcom.2018.02.251.
[39] Standard test method for adhesion strength and mechanical failure modes of ceramic coatings by quantitative single point scratch testing., (2005). https://doi.org/10.1520/C1624-05.
[40] Z. Wu, H. Bei, F. Otto, G.M. Pharr, E.P. George, Recovery, recrystallization, grain growth and phase stability of a family of FCC-structured multi-component equiatomic solid solution alloys, Intermetallics 46 (2014) 131–140, https://doi.org/10.1016/j.intermet.2013.10.024.
[41] S.G. Rao, B. Mukhamedov, G. Nagy, E.N. Tseng, R. Shu, R. Boyd, D. Primetzhofer, P.O.Å. Persson, B. Alling, I.A. Abrikosov, A. Le Febvrier, P. Eklund, Phase formation in CrFeCoNi nitride thin films, Phys. Rev. Mater. 7 (2023) 055002, https://doi.org/10.1103/PhysRevMaterials.7.055002.
[42] A.W. Hull, X-ray crystal analysis of thirteen common metals, Phys. Rev. 17 (1921) 571–588, https://doi.org/10.1103/PhysRev.17.571.
[43] H. Sawada, Residual electron density study of chromium sesquioxide by crystal structure and scattering factor refinement, Mater. Mater Res Bull 29 (1994) 239–245, https://doi.org/10.1016/0025-5408(94)90019-1.
[44] R.J. Wakelin, E.L. Yates, A study of the order-disorder transformation in iron-nickel alloys in the region $FeNi_3$, Proc. Phys. Soc. B 66 (1953) 221–240, https://doi.org/10.1088/0370-1301/66/3/310.
[45] M.K. Kini, S. Lee, A. Savan, B. Breitbach, Y. Addab, W. Lu, M. Ghidelli, A. Ludwig, N. Bozzolo, C. Scheu, D. Chatain, G. Dehm, Nanocrystalline equiatomic CoCrFeNi alloy thin films: are they single phase fcc? Surf. Coat. Technol. 410 (2021) 126945 https://doi.org/10.1016/j.surfcoat.2021.126945.
[46] J. Pelleg, Z. I.Z., L. S., Reactive-sputter-deposited TiN films on glass substrates, (1991). DOI: 10.1016/0040-6090(91)90225-M.
[47] X. Gao, M. Hu, Y. Fu, L. Weng, W. Liu, J. Sun, Low temperature deposited Ag films exhibiting highly preferred orientations, Mater. Mater. Lett. 213 (2018) 178–180, https://doi.org/10.1016/j.matlet.2017.11.074.
[48] R.E. Reed-Hill, R. Abbaschian, R. Abbaschian, Physical Metallurgy Principles, Van Nostrand, New York, 1973. http://sutlib2.sut.ac.th/sut_contents/H132782.pdf. accessed June 16, 2025.
[49] B.A. Movchan, A.V. Demchishin, Structure and properties of thick condensates of nickel, titanium, tungsten, aluminum oxides, and zirconium dioxide in vacuum, Fiz. Met. Met. 28 (1969) 653–660. Oct 1969, https://www.osti.gov/biblio/4181669.
[50] J.A. Thornton, High rate thick film growth, Annu. Rev. Mater. Sci. 7 (1977) 239–260, https://doi.org/10.1146/annurev.ms.07.080177.001323.
[51] L. Feng, Y.-Y. Ren, Y.-H. Zhang, S. Wang, L. Li, Direct correlations among the grain size, texture, and indentation behavior of nanocrystalline nickel coatings, Met 9 (2019) 188, https://doi.org/10.3390/met9020188.
[52] C. Han, Y. Zhang, J. Liu, Z. Li, Y. Wu, Y. Cui, F. Wang, Z. Liu, Effect of Mo content on microstructure and mechanical properties of CoCrFeNi Series high-entropy alloys, J. Mater. Res. Technol. 30 (2024) 8209–8217, https://doi.org/10.1016/j.jmrt.2024.05.200.
[53] Y. Shi, M.L. Falk, Stress-induced structural transformation and shear banding during simulated nanoindentation of a metallic glass, Acta Mater. 55 (2007) 4317–4324, https://doi.org/10.1016/j.actamat.2007.03.029.
[54] B.D. Beake, The influence of the H/E ratio on wear resistance of coating systems – Insights from small-scale testing, Surf. Coat. Technol. 442 (2022) 128272, https://doi.org/10.1016/j.surfcoat.2022.128272.
[55] S.J. Oh, D.C. Cook, H.E. Townsend, Characterization of iron oxides commonly formed as corrosion products on steel, Hyperfine Interact. 112 (1998) 59–66, https://doi.org/10.1023/A:1011076308501.
[56] T. Ohmi, Y. Nakagawa, M. Nakamura, A. Ohki, T. Koyama, Formation of chromium oxide on 316L austenitic stainless steel, J. Vac. Sci. Technol. 14 (1996) 2505–2510, https://doi.org/10.1116/1.580010.
[57] S.A. Arreola-Villa, H.J. Vergara-Hernández, G. Solorio-Diáz, A. Pérez-Alvarado, O. Vázquez-Gómez, G.M. Chávez-Campos, Kinetic study of oxide growth at high temperature in low carbon steel, Met 12 (2022) 147, https://doi.org/10.3390/met12010147.
[58] R.Y. Chen, W.Y.D. Yuen, Oxidation of low-carbon, low-silicon mild steel at 450–900 °C under conditions relevant to hot-strip processing, 53–79 (2002). https://doi.org/10.1023/A:1013390628475.
[59] D.S. Grebenkov, Diffusion-controlled reactions: an overview, Molecules 28 (2023) 7570, https://doi.org/10.3390/molecules28227570.